Enabling Coal-Fired Power Flexibility: Wide-Temperature NOx Removal via Strong Electron–Orbital Interaction in Dual-Site Catalysts

Shaogang Wang [1], Pengxin Zeng [2,*], Ning Li [1], Yuansheng Yi [1], Yongsheng Qin [1], Xin Yu [2], Lei Liu [2], Qi Guo [2] and Zijian Zhou [2,*]

[1] Datang International Shentou Power Generation Company Limited, Shuozhou 036000, China; dtstwsg@163.com (S.W.); lilytomato123@163.com (N.L.); yiyuansheng2025@163.com (Y.Y.); ddbb0923@163.com (Y.Q.)

[2] State Key Laboratory of Coal Combustion, School of Energy and Power Engineering, Huazhong University of Science and Technology, Wuhan 430074, China; hustyuxin@hust.edu.cn (X.Y.); liulei55@hust.edu.cn (L.L.); guoqi@hust.edu.cn (Q.G.)

* Correspondence: pancraszeng@hust.edu.cn (P.Z.); zhouzj2012@hust.edu.cn (Z.Z.)

Abstract

The narrow operating temperature window of commercial V-W/TiO$_2$ catalysts severely limits NO$_x$ removal efficiency, especially during low-load boiler operations. To achieve broad-temperature NO$_x$ abatement, we developed Ce-M/Ti (M = Co, Fe, Mn, Mo) catalysts via a dual-site strategy. The temperatures required for 80% NO conversion (T$_{80}$) were 302 °C for Ce-Mo/Ti, 372 °C for Ce-Fe/Ti, 393 °C for Ce-Mn/Ti, and 415 °C for Ce-Co/Ti. Among them, Ce-Mo/Ti exhibited the most favorable low-temperature activity, outperforming a commercial catalyst (324 °C). Its turnover frequency (3.12 × 10^{-3} s^{-1}) was 1.29 times higher. Combined physicochemical characterization and density functional theory (DFT) calculations further reveal the mechanism behind the enhanced dual-site synergy in Ce-Mo/Ti. In the Ce-Co, Ce-Fe, and Ce-Mn sites, weak orbital hybridization leads to limited charge transfer. In contrast, Ce-Mo/Ti exhibits stronger hybridization between the Ce 4f/5d and Mo 4d orbitals, which breaks the inherent limitation of the Ce-based (Ce^{3+}/Ce^{4+}) redox capability and enables reverse electron transfer from Mo to Ce. This distinctive electron transfer direction creates a unique electronic environment, activating an efficient redox cycle between Mo^{6+}/Mo^{5+} and Ce^{4+}/Ce^{3+}. This work offers a promising design strategy for dual-site catalysts with high NO$_x$ removal efficiency over a wide temperature range.

Keywords: low-temperature NH$_3$-SCR; NO$_x$ removal; synergistic dual-site; electron-orbital interaction; redox capability

1. Introduction

Nitrogen oxides (NO$_x$) are significant gaseous pollutants that cause environmental issues such as acid rain, the greenhouse effect, and photochemical smog, posing serious threats to human health [1]. Stationary sources, particularly coal-fired power plants, are major contributors to NO$_x$ emissions. Selective catalytic reduction (SCR) is one of the most mature and promising technologies for controlling NO$_x$ emissions from power plants [2,3]. Conventional commercial V$_2$O$_5$-WO$_3$/TiO$_2$ catalysts facilitate the redox reaction between NH$_3$ (as a reductant) and NO$_x$ to produce N$_2$ and H$_2$O, and are widely used in large-scale power plants [4]. However, these catalysts suffer from critical drawbacks, including poor

low-temperature activity, a narrow operating temperature window, and the biological toxicity of vanadium [5]. Against the backdrop of rapid development in renewable energy technologies, thermal power plants are increasingly required to adjust their output to accommodate the integration of renewable sources into the grid. This peak-shaving duty leads to extended operation under low-load conditions, resulting in lower flue gas temperatures at the boiler outlet. When the boiler load drops by approximately 40%, the flue gas temperature can decrease by about 60 °C, often bringing the temperature at the SCR reactor inlet below 300 °C [6,7]. Therefore, there is an urgent need to develop novel NH$_3$-SCR catalysts with excellent low-temperature activity and a broad operating window to adapt to reduced flue gas temperatures during low-load operation [8–10].

Recent research on low-temperature NH$_3$-SCR catalysts has focused mainly on supported metal oxides [11] and metal oxide solid-solution catalysts [12]. Cerium-based catalysts, known for their excellent oxygen storage capacity and significant redox properties, are frequently used as active components or supports in reactions such as the water–gas shift [13]. Previous studies have clearly shown that cerium-based active components readily generate abundant surface defects and oxygen vacancies [14], which are highly beneficial for low-temperature SCR activity [15,16]. Moreover, cerium is biologically non-toxic. Thus, environmentally friendly Ce-based catalysts with promising low-temperature performance are regarded as ideal alternatives for selective catalytic reduction of NO$_x$ over a wide temperature range. For example, Xu et al. [17] found that CeO$_2$ impregnated on TiO$_2$ support achieved NOx removal efficiency comparable to that of commercial catalysts, even in the absence of vanadium. Furthermore, CeTiO$_x$ nanotubes (CeTiO$_x$-T) synthesized via a hydrothermal method exhibited high surface Brønsted acidity and strong chemisorbed oxygen capacity [18]. However, such catalysts also have notable limitations: the redox capability of the Ce^{4+}/Ce^{3+} couple is fixed, and high loadings of CeO$_2$ can lead to excessive oxidation of NH$_3$, generating undesirable byproducts such as NO and N$_2$O. Consequently, the improvement in low-temperature activity and operating window width achieved with pure CeO$_2$-based catalysts remains limited compared to commercial systems. In catalytic reactions, redox performance refers to a catalyst's ability to donate or accept electrons (or oxygen atoms). The ease of electron transfer fundamentally determines the strength of redox capability, which in turn depends on the electronic structure of the constituent atoms. Therefore, designing the electronic structure of active sites represents a promising strategy to overcome the inherent limitations of Ce-based catalysts in redox capacity and further enhance low-temperature activity [19]. Currently, incorporating a second active component to form dual-site active centers with electronic synergy and orbital hybridization is an effective approach for electronic structure design [20,21]. Many low-cost transition metals (e.g., Co [22], Fe [23], Mn [24–26], Mo [27]) are widely used as active components or promoters in catalysts, owing to the ability of their d-orbitals to readily lose or gain electrons, facilitating orbital hybridization. Our previous work demonstrated that bimetallic sites (e.g., Fe-Co/Ti) created through strong electronic interactions can form highly active interfacial sites, surpassing the performance limitations of single-component catalysts (e.g., Fe-based catalysts) [28]. Additionally, Xin et al. [29] found that doping with transition metals can induce lattice distortion, further enhancing catalytic activity. The incorporation of more oxygen vacancies and defects also provides additional acid sites and active centers for reactant adsorption in SCR reactions [30]. For cerium-based materials, Liu et al. [31] suggested that transition metals like Co can form strongly interacting mixed bonds with Ce, acting as "electron bridges" to promote electron transfer between the two components and enhance redox capability toward nitrogen oxides. However, different transition metals (M) possess different inherent electronegativities, leading to variations in the bond strength and length of the Ce-O-M linkage in Ce-based catalysts doped with different metals. Therefore,

comparative studies on the electronic structures and catalytic activities of Ce-based catalysts doped with various transition metals are necessary.

Herein, typical transition metals (Co, Fe, Mn, Mo) were selected to design and synthesize dual-site Ce-based catalysts (Ce-Co/Ti, Ce-Fe/Ti, Ce-Mn/Ti, and Ce-Mo/Ti) via a one-step hydrothermal method, anchoring the paired sites onto a TiO_2 support. The differences in denitration activity and electronic structure among the four catalysts were systematically investigated through performance tests, physicochemical characterization, and DFT calculations. Activity evaluations revealed that Ce-Mo/Ti exhibits superior low-temperature activity and a broader operating temperature window compared to commercial V-W/Ti catalysts. Characterization and DFT results further indicated that Ce-Mo/Ti possesses a greater number and diversity of low-temperature acid sites. Moreover, it was confirmed that the introduction of Mo, compared to Co, Fe, or Mn, leads to the formation of a stronger Ce-O-Mo bond and activates more profound electronic synergy between Ce and Mo. Importantly, the key mechanism underlying the synergistic effect between Ce and Mo sites has been thoroughly elucidated.

2. Results and Discussion

2.1. Selective Catalytic Reduction Activity of Catalysts with Dual-Site

The catalytic activities of the highly dispersed dual-site catalysts prepared in this work and a commercial catalyst are compared in Figure 1. As shown in Figure 1a, the NO_x conversion of all synthesized dual-site catalysts and commercial V-W/Ti increases initially and then decreases within the temperature range of 150–450 °C. The temperatures required for 80% NO conversion (T_{80}) for Ce-Mo/Ti, Ce-Fe/Ti, Ce-Mn/Ti, and Ce-Co/Ti are 302 °C, 372 °C, 393 °C, and 415 °C, respectively. Notably, Ce-Mo/Ti exhibits superior low-temperature activity compared to commercial V-W/Ti (T_{80} = 324 °C), demonstrating the widest active temperature window. Moreover, as temperature increases from 50 to 450 °C, the N_2 selectivity of both Ce-Mo/Ti and commercial V-W/Ti declines (Figure 1b); however, the decrease for Ce-Mo/Ti is less than 2%, indicating better performance. It is worth noting that the active metal content in the commercial V-W/Ti catalyst (V = 1.40 wt%, W = 3.68 wt%) is higher than that in Ce-Mo/Ti (Ce/Mo = 1 wt% each), as confirmed by XRF analysis (Table S1). In light of the importance of denitration stability for industrial application, the Ce-Mo/Ti catalyst—which also exhibits the best low-temperature activity—was subjected to a 24 h long-term test, with the commercial V-W/Ti catalyst tested under the same conditions as a reference (Figure 1e). It is evident that the Ce-Mo/Ti catalyst maintains a high NO_x conversion of ≥79% throughout the 24 h period, demonstrating excellent stability of the designed wide-temperature-range dual-site catalyst.

To further evaluate the catalytic performance of the dual-site catalysts, the apparent activation energies (E_a) of Ce-Mo/Ti, Ce-Fe/Ti, Ce-Mn/Ti, commercial V-W/Ti, and Ce-Co/Ti were calculated and are presented in Figure 1c. Consistent with the catalytic activity trends in Figure 1a, Ce-Co/Ti shows the highest E_a (137.67 kJ/mol), while Ce-Mo/Ti exhibits the lowest (43.61 kJ/mol), suggesting that the energy barriers for key steps in the NH_3-SCR reaction are significantly reduced on Ce-Mo/Ti, facilitating low-temperature reaction kinetics. The turnover frequency (TOF), defined as the number of reactant molecules converted per active site per unit time, is a fundamental metric for intrinsic catalytic activity. The calculated TOF values for Ce-Mo/Ti, Ce-Fe/Ti, Ce-Mn/Ti, commercial V-W/Ti, and Ce-Co/Ti are 31.22×10^{-4}, 11.06×10^{-4}, 4.79×10^{-4}, 24.09×10^{-4}, and 1.03×10^{-4} s^{-1}, respectively. The TOF of Ce-Mo/Ti is approximately 1.29 times that of commercial V-W/Ti, further confirming the synergistic effect between Ce and Mo sites in enhancing low-temperature catalytic efficiency.
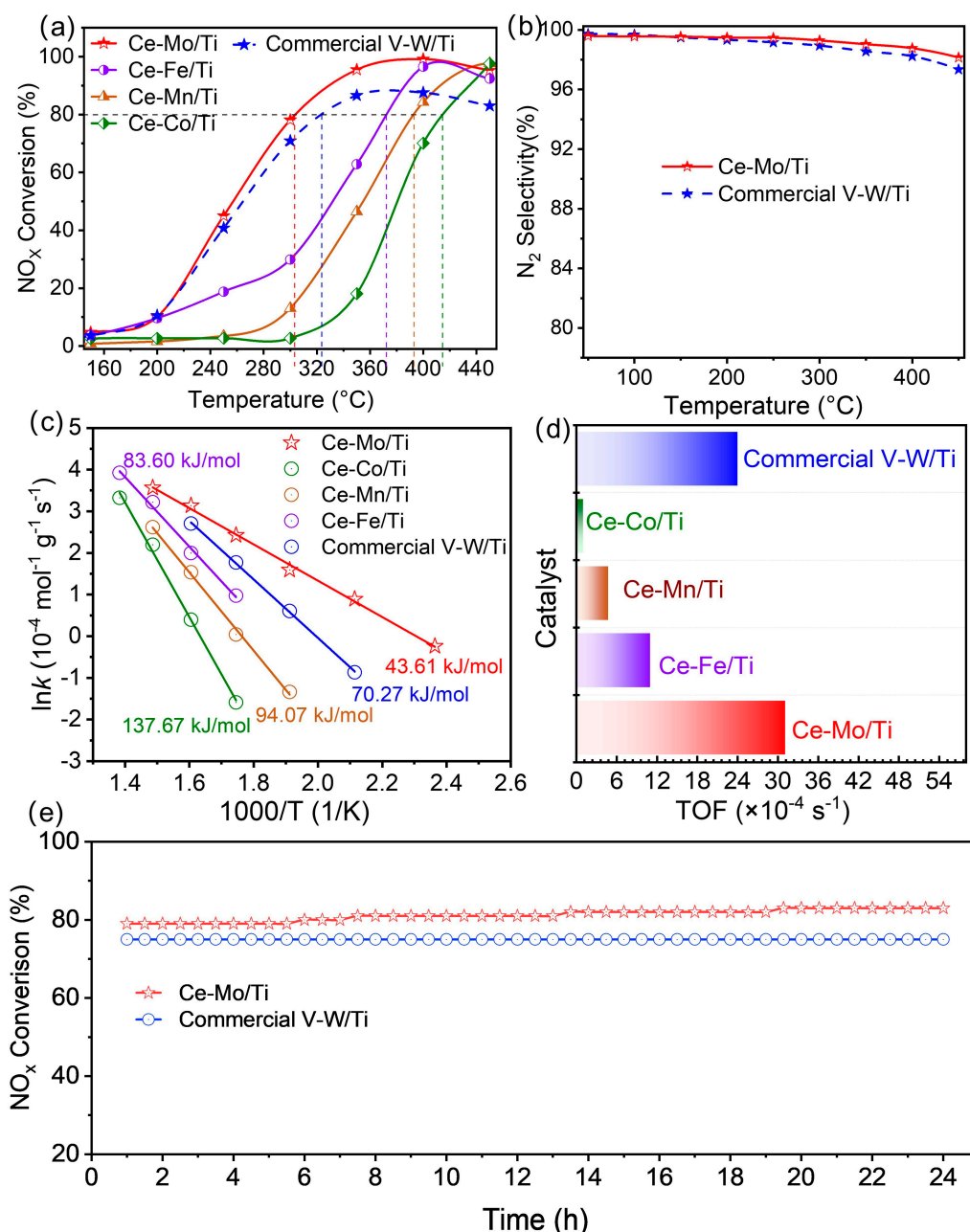
Figure 1. Catalytic activity of NH$_3$-SCR with the catalysts: (**a**) NO conversion on Ce-Mo/Ti, Ce-Fe/Ti, Ce-Mn/Ti, commercial V-W/Ti, and Ce-Co/Ti at different temperatures; (**b**) N$_2$ selectivity of Ce-Mo/Ti and commercial V-W/Ti; (**c**) Arrhenius plots of NO$_x$ conversions and (**d**) TOF in SCR over the Ce-Mo/Ti, Ce-Fe/Ti, Ce-Mn/Ti, commercial V-W/Ti, and Ce-Co/Ti; (**e**) The 24 h long-term performance comparison of Ce-Mo/Ti and commercial V-W/Ti at 300 °C; (0.5 g of catalyst, 500 ppm NO, 3% O$_2$, 500 ppm NH$_3$ and equilibrium gas N$_2$, WHSV = 60,000 h^{-1}).

Preliminary experiments on the mass ratio optimization indicate that Ce-Mo/Ti still exhibits the most potent synergistic effect even at a Ce:M (M = Mo, Fe, Mn, and Co) mass ratio of 2:1 (Figure S1). A detailed investigation into the relationship between the composition and performance will be a key focus of future work.

2.2. Comparison of Electronic Structure and Synergistic Effect of the Dual-Site Catalysts

In the XRD pattern shown in Figure 2a, the Ce-Co/Ti, Ce-Fe/Ti, Ce-Mn/Ti, and Ce-Mo/Ti catalysts all exhibit characteristic diffraction peaks corresponding to the anatase phase of TiO$_2$ (PDF#21-1272). However, no crystalline phases related to Ce-based species or

other metal oxides (such as Mo, Co, Fe, or Mn) are detected, indicating that the active species in the dual-site catalysts prepared in this work are highly dispersed on the surface of the TiO_2 support. This structural feature maximizes the exposure of active sites while maintaining the crystalline stability of TiO_2, thereby providing a foundation for catalytic reactions. NH_3-TPD profiles of Ce-Co/Ti, Ce-Fe/Ti, Ce-Mn/Ti, Ce-Mo/Ti are shown in Figure 2b, significant differences are observed in the NH_3 desorption peak temperatures among the various catalysts. The high-temperature desorption peaks for Ce-Co/Ti, Ce-Fe/Ti, and Ce-Mn/Ti are centered around 560 °C, whereas that for Ce-Mo/Ti is shifted downward to approximately 510 °C. Additionally, Ce-Mo/Ti exhibits a larger low-temperature desorption peak at around 150 °C. According to the principles of NH_3-TPD, the peak temperature reflects the strength of acid sites (higher temperature indicates stronger acidity and stronger NH_3 adsorption), while the peak profile and area reflect the distribution and quantity of acid sites [32]. For Ce-Mo/Ti, the lower desorption temperature suggests that its acid sites are predominantly medium-strong or weak, rather than strong. This moderate acid strength facilitates an efficient balance of "adsorption–desorption–activation" for reactant NH_3 in the low to medium temperature range—ensuring sufficient NH_3 adsorption on the catalyst surface to supply the reaction, while also allowing rapid desorption and activation at relatively low temperatures (e.g., forming active intermediates such as -NH_2) [33]. In contrast, catalysts like Ce-Co/Ti exhibit higher peak temperatures, indicating a greater proportion of strong acid sites. As a result, NH_3 is too strongly adsorbed to desorb and activate readily at low temperatures, thereby limiting low-temperature catalytic activity. To investigate the surface oxygen species, cerium valence states, and metal dispersion, X-ray photoelectron spectroscopy (XPS) measurements were performed. In the O 1s spectra (Figure 2c), the peaks were deconvoluted into two components: surface active oxygen (O_a), attributed to adsorbed oxygen or oxygen species adjacent to oxygen vacancies, and lattice oxygen (O_β), associated with metal–oxygen bonds in the crystal lattice. The proportion of O_α follows the order: Ce-Mo/Ti (18.22%) > Ce-Fe/Ti (18.09%) > Ce-Mn/Ti (17.28%) > Ce-Co/Ti (16.46%). A higher O_α content suggests a greater abundance of oxygen vacancies, which promotes the adsorption and activation of reactants in NH_3-SCR reactions [34]. The Ce 3d spectra (Figure 2f) exhibit characteristic peaks corresponding to Ce^{4+} (denoted as u, u″, u‴, v, v″, v‴, u, u″, u‴, v, v″, v‴) and Ce^{3+} (u′, v′, u′, v′). The presence of Ce^{3+} arises from the reduction process $Ce^{4+} + e^- \rightarrow Ce^{3+}$, accompanied by the formation of oxygen vacancies. The relative concentration of Ce^{3+} reflects the redox activity of cerium, specifically the efficiency of the $Ce^{3+} \leftrightarrow Ce^{4+}$ redox cycle [35]. The calculated Ce^{3+} percentages follow the sequence: Ce-Mo/Ti (11.43%) > Ce-Fe/Ti (10.67%) > Ce-Mn/Ti (10.47%) > Ce-Co/Ti (9.08%), indicating that Ce-Mo/Ti possesses the strongest redox capability, thereby facilitating electron transfer and reactant activation during catalytic processes. Notably, Ce-Mo/Ti exhibits the highest proportions of O_α and Ce^{3+}, implying the most abundant oxygen vacancies and the strongest redox capability, which collectively contribute to its superior catalytic performance.

With respect to metal dispersion, the high dispersion is further corroborated by the distinct XPS signals of Mo 3d (Figure 2g), Fe 2p (Figure 2h), Mn 2p (Figure 2e), and Co 2p (Figure 2d). Such dispersion enhances the number of accessible active sites and promotes synergistic interactions among the metal species, cerium, and the TiO_2 support, thereby modulating oxygen vacancy formation and cerium valence states.
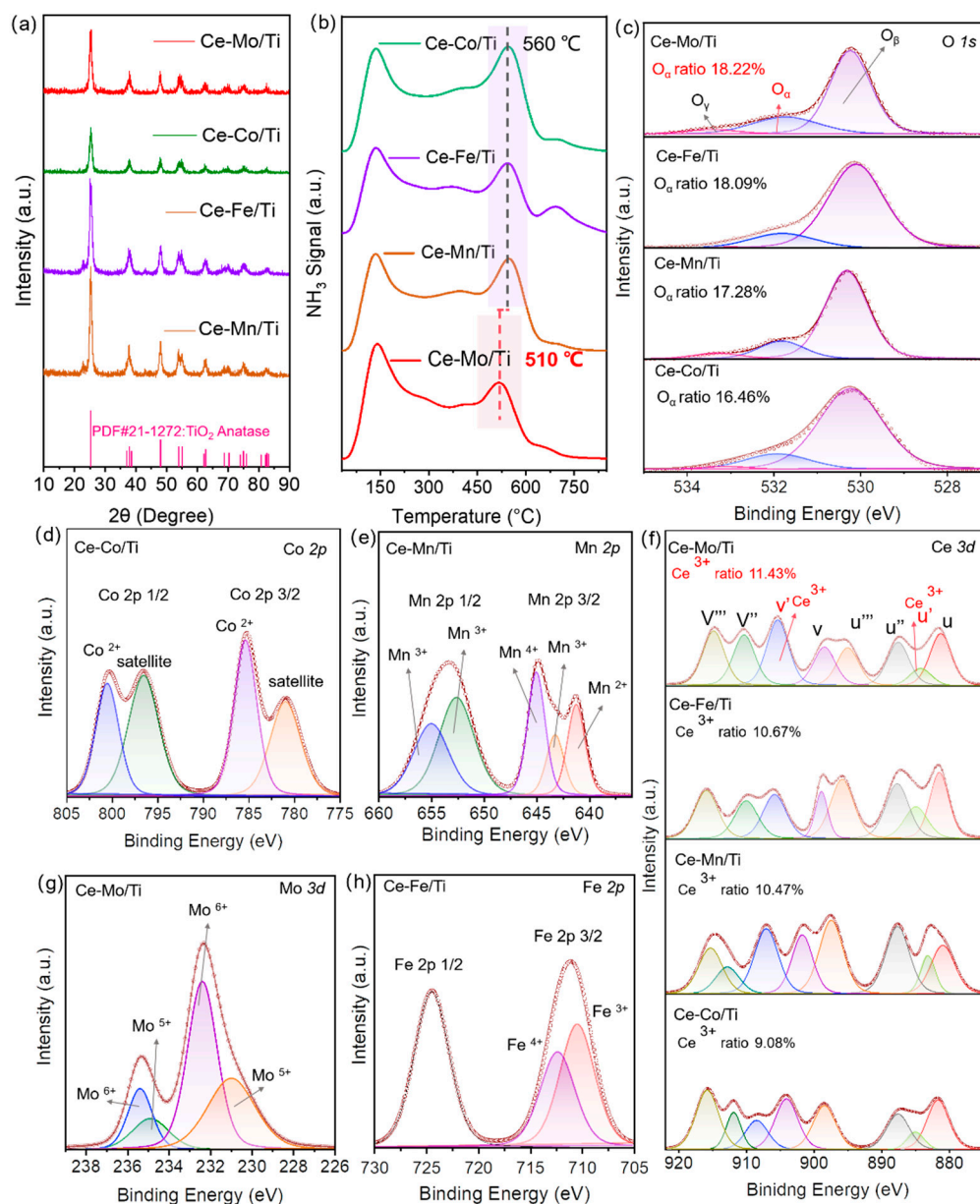
Figure 2. (**a**) The XRD diagram, (**b**) NH$_3$-TPD profiles, (**c**) O 1s XPS, (**d**) Co 2p XPS, (**e**) Mn 2p XPS, (**f**) Ce 3d XPS, (**g**) Mo 3d XPS and (**h**) Fe 2p XPS spectra of Ce-Co/Ti, Ce-Fe/Ti, Ce-Mn/Ti, Ce-Mo/Ti.

In addition, the textural properties of the Ce-Mo/Ti, Ce-Fe/Ti, Ce-Mn/Ti, and Ce-Co/Ti catalysts were evaluated using N$_2$ adsorption–desorption measurements. As depicted in Figure S2a, all samples exhibit type IV isotherms with distinct hysteresis loops, confirming their mesoporous nature. Among them, Ce-Mo/Ti shows a higher N$_2$ uptake at medium-to-high relative pressures (P/P$_0$), implying enhanced nitrogen adsorption capability attributable to its optimized pore structure. According to the BET results (Figure S2b), Ce-Mo/Ti possesses the largest specific surface area and a relatively high pore volume compared to the other catalysts. These properties are advantageous for the NH$_3$-SCR reaction, as a larger surface area offers more active sites, while a greater pore volume promotes the diffusion and transport of reactive species. In addition, the pore size distribution profiles (Figure S2c) indicate the dominant presence of micropores and mesopores in all catalysts. In summary, Ce-Mo/Ti exhibits superior textural characteristics—including a higher specific surface area, larger pore volume, and favorable pore structure—which collectively contribute to its enhanced catalytic performance in NH$_3$-SCR.

To further elucidate the structure–performance relationship of the dual-site catalysts prepared in this work, density functional theory (DFT) calculations were performed for Ce-Co/Ti, Ce-Fe/Ti, Ce-Mn/Ti, and Ce-Mo/Ti models. The optimized configurations and corresponding binding energies between the active components and the TiO_2 support are summarized in Figure 3. Given that Ce-M (M = Co, Fe, Mn and Mo) dual sites may occupy different positions on the TiO_2 support—such as shoulder or central sites—as illustrated in Figure S3, multiple configurations of the Ce-M/Ti catalyst were considered. Comparative analysis revealed that the central-site configuration represents the most stable structure for the Ce-M dual-site catalyst. Therefore, all subsequent discussions will be based on this optimal configuration. Comparative analysis of the optimized structures reveals that the Ce-Mo/Ti model (Figure 3e,f) exhibits a shorter atomic distance between Ce and Mo, suggesting more pronounced bonding and stronger electronic interaction between the two sites. As can be known from previous studies, enhanced electronic coupling may facilitate the redox cycle between Ce^{3+}/Ce^{4+} and Mo^{6+}/Mo^{5+}, thereby promoting NH_3 activation (e.g., generating -NH_2 intermediates) and NO_x reduction (by supplying active oxygen species). In contrast, the electronic interactions between Ce and Co, Fe, or Mn are relatively moderate, resulting in less efficient electron transfer. Furthermore, the incorporation of Mo induces notable lattice distortion in the TiO_2 support of Ce-Mo/Ti, which favors the formation and enrichment of oxygen vacancies or defect sites. These defects can serve as adsorption sites for NH_3 and enhance the redox properties of the catalyst. The binding energy between the active components and the support is a key computational indicator reflecting the overall structural stability of the catalyst. The calculated binding energies for Ce-Co/Ti, Ce-Fe/Ti, Ce-Mn/Ti, and Ce-Mo/Ti are -3.25, -2.25, -4.02, and -4.37 eV, respectively, indicating particularly strong interactions between the Ce-Mo/Mn and the TiO_2 support. Such strong interactions effectively stabilize the active centers, promote synergistic effects between dual sites, and inhibit sintering-induced deactivation during reaction conditions.
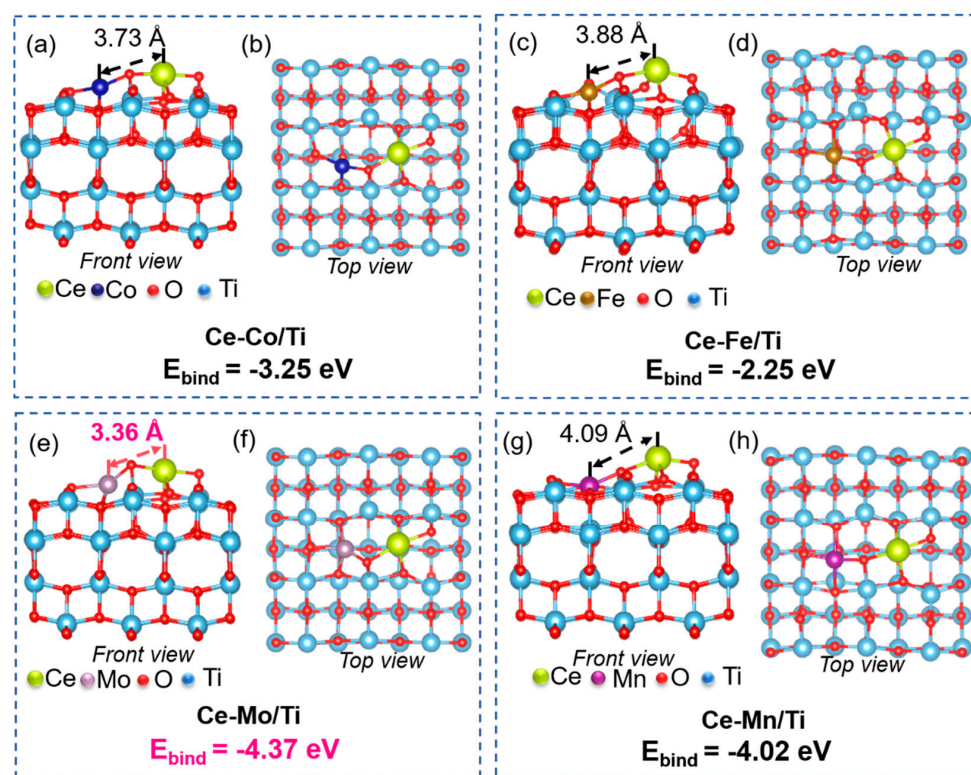

Figure 3. The optimized configurations and binding energies between active components and TiO_2 support of (**a**,**b**) Ce-Co/Ti, (**c**,**d**) Ce-Fe/Ti, (**e**,**f**) Ce-Mo/Ti, (**g**,**h**) Ce-Mn/Ti catalysts.

To investigate the electronic structure and orbital hybridization of the dual-site catalysts designed in this study, the density of states (DOS) was calculated for the four catalysts, as shown in Figure 4. Figure 4a presents the total DOS spectra and the d-band center positions of the active atoms in Ce-Co/Ti, Ce-Fe/Ti, Ce-Mn/Ti, and Ce-Mo/Ti. The calculated d-band center values are, from top to bottom: Ce-Co/Ti (Ce: -4.68 eV, Co: -1.25 eV), Ce-Fe/Ti (Ce: -3.96 eV, Fe: -0.72 eV), C-Mn/Ti (Ce: -4.47 eV, Mn:-2.58 eV), and Ce-Mo/Ti (Ce: -1.48 eV, Mo: -0.53 eV). Compared to the Fermi level ($E_f = 0$ eV), both Mo and Ce in Ce-Mo/Ti exhibit d-band centers notably closer to E_f. This indicates enhanced delocalization of d-orbital electrons in Mo and Ce, which not only optimizes the adsorption energy of NH_3/NO but also strengthens the redox coupling between Ce^{3+}/Ce^{4+} and Mo^{6+}/Mo^{5+} [36].
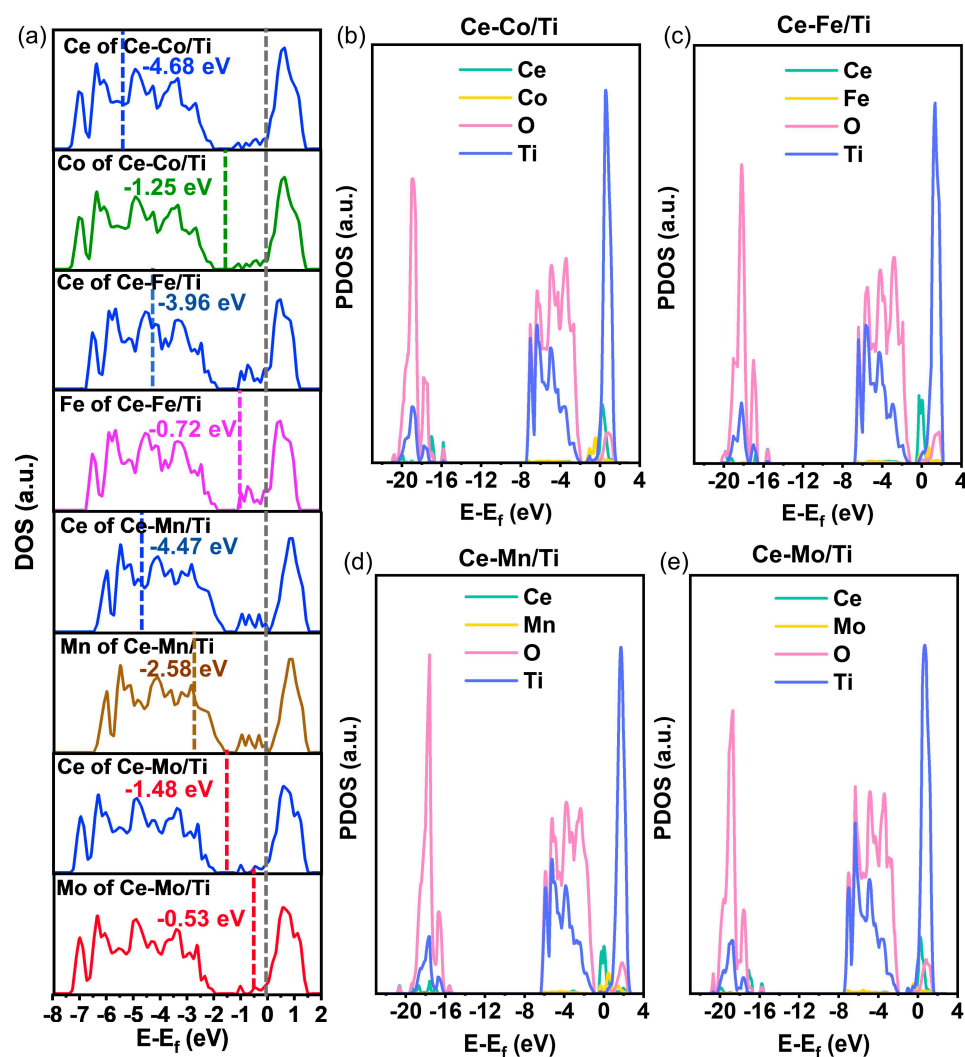

Figure 4. (**a**) DOS spectra and the d-band center positions of the active atoms in Ce-Co/Ti, Ce-Fe/Ti, Ce-Mn/Ti, and Ce-Mo/Ti; (**b–e**) PDOS spectra of each element in Ce-Co/Ti, Ce-Fe/Ti, Ce-Mn/Ti, and Ce-Mo/Ti.

Figure 4b–e display the projected density of states (PDOS) of individual elements in Ce-Co/Ti, Ce-Fe/Ti, Ce-Mn/Ti, and Ce-Mo/Ti, respectively. In comparison, Ce-Mo/Ti exhibits distinct orbital hybridization features. First, the 4*d* orbitals of Mo show a significantly higher density of states near the Fermi level than those of Co, Fe, and Mn, highlighting the advantage of Mo in regulating electron exchange with adsorbates, thereby facilitating reactant adsorption and activation [37,38]. Second, the 4*f* orbitals of Ce in Ce-Mo/Ti exhibit a richer density of states around E_f, which likely enhances its redox activity and promotes

the regeneration of active oxygen species (e.g., O^-, O_2^-). Furthermore, strong orbital hybridization between Ti and Ce/Mo reflects a robust interaction between the support and active components, optimizing electron transfer pathways [39].

2.3. Mechanism of Strong Electronic–Orbital Interaction of the Dual-Site Catalysts

Figure 5 presents the charge density difference (Figure 5a) and bader charge analysis (Figure 5b), which reveal significant differences in the electronic structures of the four catalysts and their regulatory effects on catalytic performance. In the charge density difference plots, regions of electron accumulation and depletion are represented in blue and red, respectively. Notable differences in charge transfer and redistribution are observed among the catalysts. Specifically, Ce-Mo/Ti exhibits a significantly higher and more localized charge density redistribution between the Ce and Mo active sites. In contrast, the charge density differences in Ce-Co/Ti, Ce-Fe/Ti, and Ce-Mn/Ti appear relatively sparse and diffuse. Bader charge analysis provides a quantitative assessment of these trends. In Ce-Co/Ti, the Ce site loses 0.44 e, while Co gains 0.44 e, becoming positively charged. Similarly, in Ce-Fe/Ti and Ce-Mn/Ti, Fe or Mn accepts electrons donated by Ce. Thus, Ce-Co/Ti, Ce-Fe/Ti, and Ce-Mn/Ti all follow a consistent 'Ce $\rightarrow$ transition metal' electron transfer pathway, with nearly symmetric charge exchange. This behavior can be attributed to the higher electronegativity of Co, Fe, and Mn (ranging from 1.55 to 1.88) compared to Ce (1.12), which drives electron donation from Ce to the transition metal. Interestingly, Ce-Mo/Ti demonstrates a completely opposite electron transfer direction: electrons are transferred from Mo to Ce, with Ce gaining 1.20 e and Mo losing 1.20 e—a magnitude ~3 times greater than that in the other catalysts. Although Mo has a much higher electronegativity (2.16) than Ce, strong hybridization between the Mo $4d$ and Ce $4f/5d$ orbitals leads to pronounced electron delocalization, overriding the electronegativity-driven trend and resulting in this reverse charge transfer [34].

The direction and extent of electron transfer are ultimately determined by the interplay between electronegativity and orbital hybridization [40]. In Ce-Co/Ti, Ce-Fe/Ti, and Ce-Mn/Ti, electronegativity dominates the electron flow, and hybridization between the dual sites is weak, resulting in limited charge transfer. In contrast, for Ce-Mo/Ti, strong orbital hybridization—evidenced by high charge density—outweighs the electronegativity effect, inducing reverse electron transfer. The larger number of electrons transferred facilitates an efficient redox cycle between Mo^{6+}/Mo^{5+} and Ce^{4+}/Ce^{3+}. At low temperatures, Mo acts as an electron donor ($Mo^{6+} \rightarrow Mo^{5+}$), while Ce accepts electrons ($Ce^{4+} \rightarrow Ce^{3+}$). The resulting Ce^{3+} species, with its unoccupied orbitals, efficiently adsorbs and activates NH_3 [41]. At moderate temperatures, Mo^{5+}/Mo^{4+} supplies active oxygen species, and Ce^{4+} facilitates NO oxidation, thereby supporting broad-temperature catalytic activity. This unique electronic structure modulation correlates well with the broad-temperature NH_3-TPD activity and the distinctive d-band center features observed in the DOS analysis, providing deep electronic-level insight into the superior low-temperature SCR performance of Ce-Mo/Ti.

In Figure 6, the adsorption configurations of NH_3 and NO on the active sites of the Ce-Co/Ti, Ce-Fe/Ti, Ce-Mn/Ti, and Ce-Mo/Ti catalysts are presented. The modeling study commenced with the construction of NO and NH_3 adsorption configurations at various potential sites on the Ce-M/Ti (M = Co, Fe, Mn and Mo) surface (Figures S4 and S5). Comparative analysis of the configuration energies indicated that the most stable adsorption occurs when NO or NH_3 binds directly to the metal sites (Ce or M), rather than to adjacent oxygen atoms on the Ce-M/Ti surface. The adsorption energies were systematically calculated to elucidate the structure–activity relationship governing NH_3/NO adsorption behavior and reaction mechanisms. As widely recognized, in the Eley–Rideal (E-R) mecha-

nism, NH_3 is adsorbed on an active site and converted into intermediate species such as NH_2, whereas in the Langmuir–Hinshelwood (L-H) mechanism, both NO and NH_3 are co-adsorbed on adjacent sites before reacting. These two mechanisms are schematically represented in Figure 6 by blue (E-R) and red (L-H) lines, respectively. Since each catalyst possesses dual active sites, four possible adsorption configurations were considered for each system, as illustrated in Figure 6a–d. Comparative analysis reveals that Ce-Mo/Ti exhibits significantly stronger adsorption stability, as reflected in the absolute adsorption energy values for both single NH_3 adsorption at the Ce site (-0.96 eV) and co-adsorption with NH_3 at the Mo site and NO at the Ce site (-5.66 eV), which are notably higher than those of Ce-Co/Ti, Ce-Fe/Ti, and Ce-Mn/Ti.
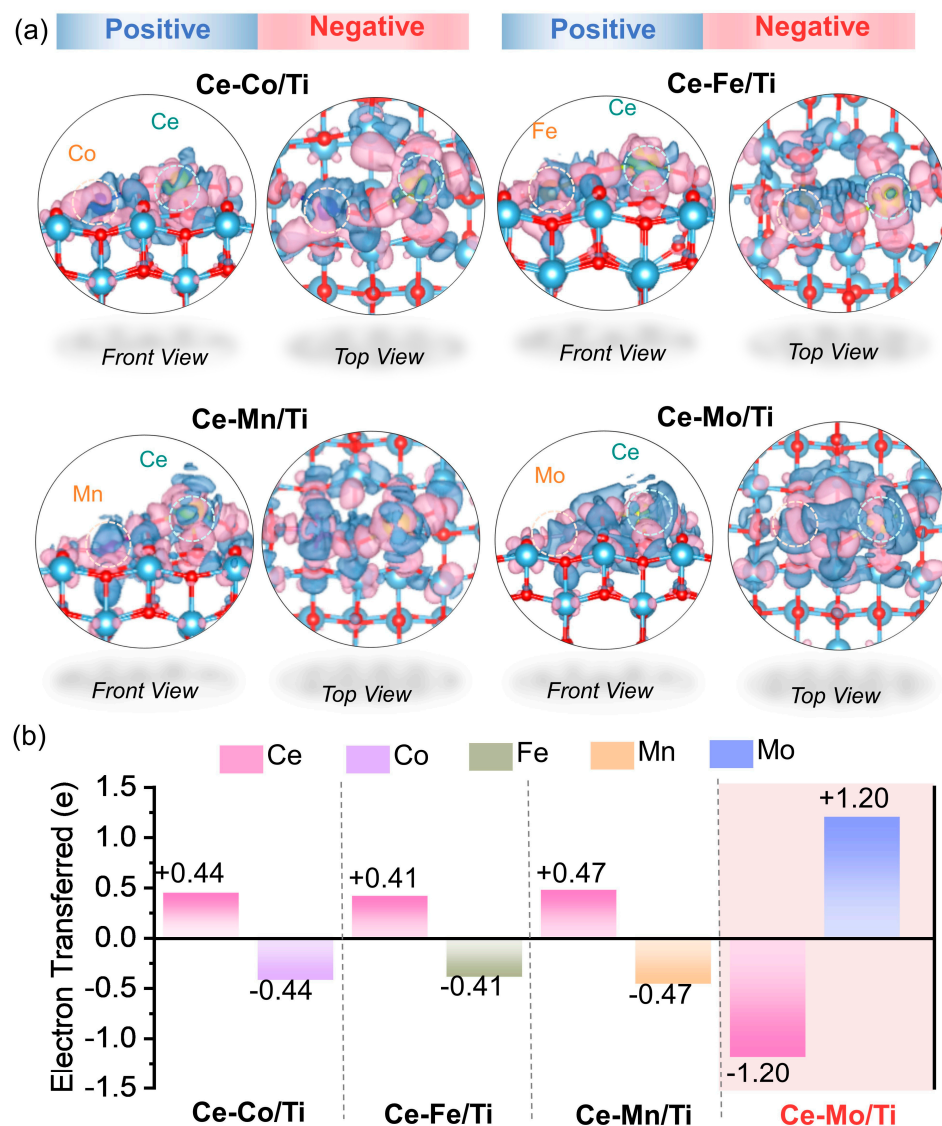

Figure 5. (**a**) The charge density difference and (**b**) bader charge analysis of Ce-Co/Ti, Ce-Fe/Ti, Ce-Mn/Ti and Ce-Mo/Ti.

This enhanced adsorption can be attributed to the unique electronic properties of Ce-Mo/Ti. As illustrated in Figure 5, the reverse electron transfer results in electron enrichment at the Ce site, enabling effective capture of the lone pair electrons of NH_3 via Lewis acid–base interaction. In the co-adsorption configuration, NO (electron-deficient acceptor) adsorbs on the electron-rich Ce site (electron donor), while NH_3 (electron-rich donor) adsorbs on the electron-deficient Mo site (acceptor). This charge complementarity enhances co-adsorption stability and reduces the energy barrier for adsorption. In contrast, in Ce-

Co/Ti, Ce-Fe/Ti, and Ce-Mn/Ti, the Ce site becomes electron-deficient due to conventional electron transfer, reducing its ability to donate electrons to NO. Meanwhile, the transition metal sites (Co/Fe/Mn) become electron-rich, which is electrostatically unfavorable for accepting electrons from NH_3. These mismatches lead to weaker adsorption and lower stability [28].
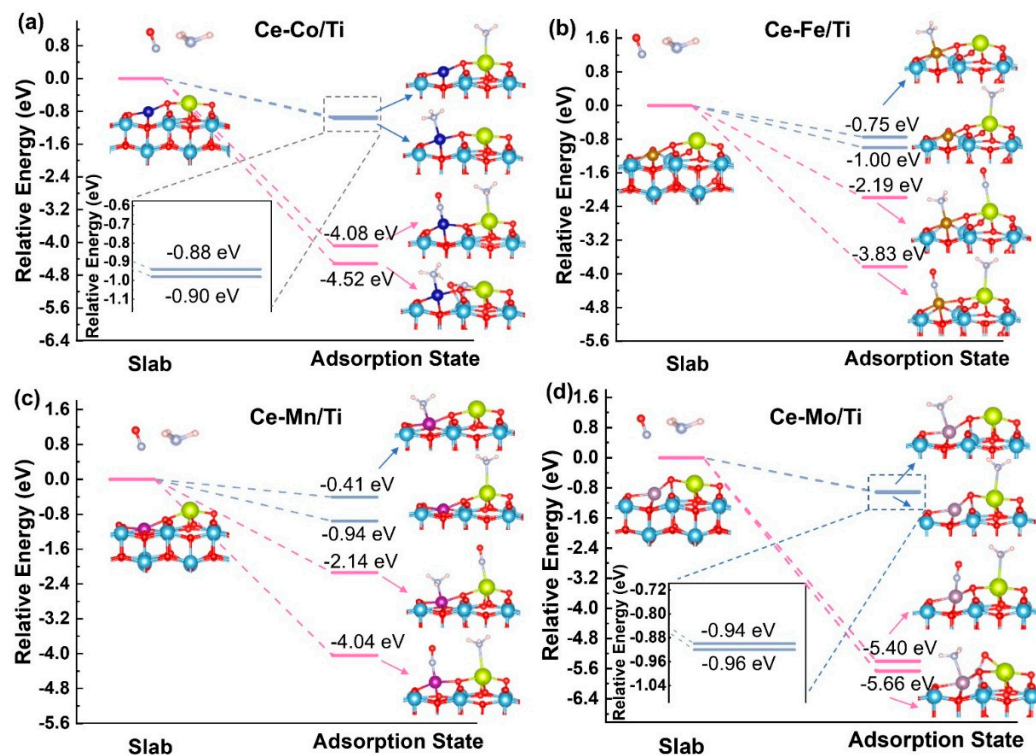

Figure 6. The adsorption configurations and adsorption energies of NH_3 and NO on the active sites of (**a**) Ce-Co/Ti, (**b**) Ce-Fe/Ti, (**c**) Ce-Mn/Ti, and (**d**) Ce-Mo/Ti.

In summary, the distinct charge distribution in Ce-Mo/Ti optimally aligns with the electronic properties of the reactants: NO as an electron acceptor and NH_3 as an electron donor. This facilitates both E-R (via NH_3 activation) and L-H (via synergistic co-adsorption) pathways. The efficient coupling of reactant adsorption at the dual sites enhances the broad-temperature SCR activity of Ce-Mo/Ti, consistent with the previously discussed electronic structure, acidic properties, and charge transfer analyses, thereby forming a coherent theoretical framework.

3. Experimental Section

3.1. Catalyst Preparation

Titanium oxysulfate ($TiOSO_4$, >99.9%) and nitric acid (HNO_3, >99.9%) were obtained from Sinopharm Chemical Reagent Co., Ltd. (Shanghai, China). Ammonium heptamolybdate tetrahydrate (($NH_4)_6Mo_7O_{24} \cdot 4H_2O$) was purchased from Aladdin Industrial Corporation (Shanghai, China). Cobalt nitrate hexahydrate ($Co(NO_3)_2 \cdot 6H_2O$, >99.5%), iron nitrate nonahydrate ($Fe(NO_3)_3 \cdot 9H_2O$, >99.5%), and cerium nitrate hexahydrate ($Ce(NO_3)_3 \cdot 6H_2O$, >99.0%) were sourced from Macklin Biochemical Co., Ltd. (Shanghai, China).

The Ce-M/Ti (M = Co, Fe, Mn, Mo) catalysts were synthesized via a one-step hydrothermal method [42]. Taking Ce-Mo/Ti as an example, the detailed procedure is described as follows. Titanium oxysulfate was used as the precursor for the TiO_2 support. Specifically, 5 g of titanium oxysulfate was dissolved in 50 mL of deionized water under stirring at room temperature for 4 h, resulting in a clear solution denoted as Solution

A. Separately, stoichiometric amounts of ammonium molybdate ($(NH_4)_6Mo_7O_{24} \cdot 4H_2O$) and cerium nitrate ($Ce(NO_3)_3 \cdot 6H_2O$) (with a Ce:Mo mass ratio of 1:1) were dissolved in deionized water. Nitric acid was added dropwise to this mixture until the pH reached 1.2, forming Solution B. Solution B was then gradually introduced into Solution A under continuous stirring for 30 min. The resulting mixture was transferred into a 150 mL Teflon-lined autoclave and subjected to hydrothermal treatment at 180 °C for 4 h. After natural cooling, the solid product was collected via high-speed centrifugation, washed repeatedly with ethanol and deionized water, dried overnight at 80 °C, and finally calcined at 450 °C for 3 h in air. The obtained catalyst, with a nominal Ce:Mo mass ratio of 1:1, is designated as Ce-Mo/Ti.

The same procedure was applied to synthesize Ce-Co/Ti, Ce-Fe/Ti, and Ce-Mn/Ti, with the transition metal precursors substituted by cobalt nitrate ($Co(NO_3)_3 \cdot 6H_2O$), ferric nitrate ($Fe(NO_3)_3 \cdot 9H_2O$), and manganese nitrate ($Mn(NO_3)_2 \cdot 4H_2O$), respectively. A commercial V_2O_5-WO_3/TiO_2 catalyst, denoted as commercial V-W/Ti, was obtained from a coal-fired power plant for comparison. Its compositional details are provided in the Supporting Information.

3.2. Catalyst Characterization and Catalytic Evaluation

The details of catalytic characterization and catalytic evaluation are shown in the Supporting Information.

3.3. DFT Calculations

The calculation details are shown in the Supporting Information.

4. Conclusions

In this study, a series of dual-site catalysts (Ce-Co, Ce-Fe, Ce-Mn, and Ce-Mo) anchored on a TiO_2 support were synthesized via a one-step hydrothermal method, with the aim of enhancing low-temperature catalytic activity. The denitration performance, electronic structure, and reactant adsorption behavior of the four catalysts were systematically investigated through activity tests, physicochemical characterization, and density functional theory (DFT) calculations. Significant differences were observed among them. The Ce-Mo/Ti catalyst exhibited the best low-temperature activity and the widest operating temperature window, achieving 80% NO_x conversion (T_{80}) at 302 °C, which is notably lower than that of a commercial V-W/Ti catalyst. Moreover, the turnover frequency (TOF) of Ce-Mo/Ti reached 3.12×10^{-3} s^{-1}, approximately 1.29 times that of the commercial catalyst (2.41×10^{-3} s^{-1}), confirming the synergistic effect between Ce and Mo sites in promoting low-temperature efficiency. Compared with Ce-Co/Ti, Ce-Fe/Ti, and Ce-Mn/Ti, the Ce-Mo/Ti catalyst possessed more abundant surface acid sites at low temperatures. Most importantly, electron transfer in Ce-Co/Ti, Ce-Fe/Ti, and Ce-Mn/Ti was primarily governed by electronegativity, resulting in limited orbital hybridization and charge transfer between the dual sites. In contrast, Ce-Mo/Ti exhibited strong orbital hybridization, as evidenced by high charge density, overriding electronegativity-driven trends and inducing reverse electron transfer. In this case, Mo acts as an electron donor ($Mo^{6+} \rightarrow Mo^{5+}$), while Ce serves as an electron acceptor ($Ce^{4+} \rightarrow Ce^{3+}$). Consequently, the increased concentration of Ce^{3+} species—with their partially unoccupied orbitals—enables efficient adsorption and activation of NH_3 at low temperatures. Furthermore, the unique charge distribution in Ce-Mo/Ti optimally aligns with the electronic properties of the reactants, leading to superior NO/NH_3 adsorption performance. This work demonstrates a promising strategy for designing dual-site catalysts and elucidates the synergistic mechanisms, offering valu-

able insights for the development of high-performance selective catalytic reduction (SCR) catalysts with broad operating temperature windows.

Supplementary Materials: The following supporting information can be downloaded at https://www.mdpi.com/article/10.3390/catal15100971/s1. Table S1: XRF results of commercial V-W/Ti catalyst; Figure S1: NO_x conversion on Ce-Mo/Ti, Ce-Fe/Ti, Ce-Mn/Ti, and Ce-Co/Ti at different temperatures (mass ratio of Ce:M = 2:1); Figure S2: The textural properties of the Ce-Mo/Ti, Ce-Fe/Ti, Ce-Mn/Ti, and Ce-Co/Ti catalysts: (a) adsorption and desorption curves, (b) BET specific surface areas and BJH pore volumes, and (c) pore size distribution plots of the catalysts; Figure S3: DFT configuration of Ce-M at different positions of Ce-M/Ti (M = Co, Fe, Mn, Mo); Figure S4: The adsorption configuration of NO at different active sites on Ce-M/Ti (M = Co, Fe, Mn, Mo); Figure S5: The adsorption configuration of NH_3 at different active sites on Ce-M/Ti (M = Co, Fe, Mn, Mo).

Author Contributions: Conceptualization, Z.Z.; Methodology, Q.G. and N.L.; Software, Y.Y.; Validation, Y.Q.; Investigation, L.L. and X.Y.; Writing—review and editing, S.W. and P.Z.; Supervision, Z.Z. All authors have read and agreed to the published version of the manuscript.

Data Availability Statement: Data are contained within the article and Supplementary Materials.

Conflicts of Interest: Authors Shaogang Wang, Ning Li, Yuansheng Yi and Yongsheng Qin were employed by the company Datang International Shentou Power Generation Company Limited. The remaining authors declare that the research was conducted in the absence of any commercial or financial relationships that could be construed as a potential conflict of interest.

References

1. Han, L.; Cai, S.; Gao, M.; Hasegawa, J.Y.; Wang, P.; Zhang, J.; Shi, L.; Zhang, D. Selective Catalytic Reduction of NO_x with NH_3 by Using Novel Catalysts: State of the Art and Future Prospects. *Chem. Rev.* **2019**, *119*, 10916–10976. [CrossRef] [PubMed]
2. Lian, Z.; Wei, J.; Shan, W.; Yu, Y.; Radjenovic, P.M.; Zhang, H.; He, G.; Liu, F.; Li, J.F.; Tian, Z.Q.; et al. Adsorption-Induced Active Vanadium Species Facilitate Excellent Performance in Low-Temperature Catalytic NO_x Abatement. *J. Am. Chem. Soc.* **2021**, *143*, 10454–10461. [CrossRef] [PubMed]
3. Liu, J.; Shi, X.; Yu, Y.; Zhang, M.; Liu, D.; He, H. Excellent hydrocarbon tolerance of CeO_2-WO_3-SnO_2 oxide catalyst for the NH_3-SCR of NO_x. *Appl. Catal. B Environ.* **2023**, *324*, 122283. [CrossRef]
4. Kwon, D.W.; Kim, D.H.; Lee, S.; Kim, J.; Ha, H.P. A dual catalytic strategy by the nature of the functionalization effect as well as active species on vanadium-based catalyst for enhanced low temperature SCR. *Appl. Catal. B Environ.* **2021**, *289*, 120032. [CrossRef]
5. Liu, J.; He, G.; Shan, W.; Yu, Y.; Huo, Y.; Zhang, Y.; Wang, M.; Yu, R.; Liu, S.; He, H. Introducing tin to develop ternary metal oxides with excellent hydrothermal stability for NH_3 selective catalytic reduction of NO_x. *Appl. Catal. B Environ.* **2021**, *291*, 120125. [CrossRef]
6. Li, Y.; Li, G.; Zou, Y.; Liu, W.; Zhang, H.; Lu, S.; Li, Z.; Zhang, S.; Peng, H. Unveiling the remarkable $deNO_x$ performance of $MnMoVO_x$ catalysts via dual regulation of the redox and acid sites. *Appl. Catal. B Environ. Energy* **2024**, *344*, 123612. [CrossRef]
7. Zhou, Z.-J.; Liu, X.-W.; Zhao, B.; Chen, Z.-G.; Shao, H.-Z.; Wang, L.-L.; Xu, M.-H. Effects of existing energy saving and air pollution control devices on mercury removal in coal-fired power plants. *Fuel Process. Technol.* **2015**, *131*, 99–108. [CrossRef]
8. Usberti, N.; Jablonska, M.; Blasi, M.D.; Forzatti, P.; Lietti, L.; Beretta, A. Design of a "high-efficiency" NH_3-SCR reactor for stationary applications. A kinetic study of NH_3 oxidation and NH_3-SCR over V-based catalysts. *Appl. Catal. B Environ.* **2015**, *179*, 185–195. [CrossRef]
9. Li, G.; Wang, B.; Ma, Z.; Wang, H.; Ma, J.; Zhao, C.; Zhou, J.; Lin, D.; He, F.; Han, Z.; et al. Aluminium-induced component engineering of mesoporous composite materials for low-temperature NH_3-SCR. *Commun. Chem.* **2020**, *3*, 66. [CrossRef]
10. He, G.; Lian, Z.; Yu, Y.; Yang, Y.; Liu, K.; Shi, X.; Yan, Z.; Shan, W.; He, H. Polymeric vanadyl species determine the low-temperature activity of V-based catalysts for the SCR of NO_x with NH_3. *Sci. Adv.* **2018**, *4*, eaau4637. [CrossRef] [PubMed]

11. Hu, X.; Huang, L.; Zhang, J.; Li, H.; Zha, K.; Shi, L.; Zhang, D. Facile and template-free fabrication of mesoporous 3D nanosphere-like $Mn_xCo_{3-x}O_4$ as highly effective catalysts for low temperature SCR of NO_x with NH_3. *J. Mater. Chem. A* **2018**, *6*, 2952–2963. [CrossRef]

12. Sreekanth, P.M.; Peña, D.A.; Smirniotis, P.G. Titania Supported Bimetallic Transition Metal Oxides for Low-Temperature SCR of NO with NH_3. *Ind. Eng. Chem. Res.* **2006**, *45*, 6444–6449. [CrossRef]

13. Farrauto, R.; Hwang, S.; Shore, L.; Ruettinger, W.; Lampert, J.; Giroux, T.; Liu, Y.; Ilinich, O. New Material Needs for Hydrocarbon Fuel Processing: Generating Hydrogen for the PEM Fuel Cell. *Annu. Rev. Mater. Res.* **2003**, *33*, 1–27. [CrossRef]

14. Campbell, C.T.; Peden, C.H.F. Oxygen Vacancies and Catalysis on Ceria Surfaces. *Science* **2005**, *309*, 713–714. [CrossRef]

15. Wu, Z.; Li, M.; Overbury, S.H. On the structure dependence of CO oxidation over CeO_2 nanocrystals with well-defined surface planes. *J. Catal.* **2012**, *285*, 61–73. [CrossRef]

16. Li, Q.; Li, X.; Li, W.; Zhong, L.; Zhang, C.; Fang, Q.; Chen, G. Effect of preferential exposure of anatase TiO_2 {0 0 1} facets on the performance of Mn-Ce/TiO_2 catalysts for low-temperature selective catalytic reduction of NO_x with NH_3. *Chem. Eng. J.* **2019**, *369*, 26–34. [CrossRef]

17. Xu, W.; Yu, Y.; Zhang, C.; He, H. Selective catalytic reduction of NO by NH_3 over a Ce/TiO_2 catalyst. *Catal. Commun.* **2008**, *9*, 1453–1457. [CrossRef]

18. Zhang, Z.; Li, R.; Wang, M.; Li, Y.; Tong, Y.; Yang, P.; Zhu, Y. Two steps synthesis of $CeTiO_x$ oxides nanotube catalyst: Enhanced activity, resistance of SO_2 and H_2O for low temperature NH_3-SCR of NO_x. *Appl. Catal. B Environ.* **2021**, *282*, 119542. [CrossRef]

19. Fang, X.; Qu, W.; Qin, T.; Hu, X.; Chen, L.; Ma, Z.; Liu, X.; Tang, X. Abatement of Nitrogen Oxides via Selective Catalytic Reduction over $Ce_1–W_1$ Atom-Pair Sites. *Environ. Sci. Technol.* **2022**, *56*, 6631–6638. [CrossRef]

20. Yang, Z.; Song, J.; Zhang, G.; Sun, X.; Cheng, S.; Zhang, X.; Jiang, Y. Unraveling the promotion for SO_2 and H_2O resistance of transition metal-doped CeO_2-TiO_2 catalysts in NH_3-SCR reaction: A DFT study. *J. Hazard. Mater.* **2025**, *489*, 137563. [CrossRef]

21. Qu, W.; Liu, X.; Chen, J.; Dong, Y.; Tang, X.; Chen, Y. Single-atom catalysts reveal the dinuclear characteristic of active sites in NO selective reduction with NH_3. *Nat. Commun.* **2020**, *11*, 1532. [CrossRef] [PubMed]

22. Meng, D.; Xu, Q.; Jiao, Y.; Guo, Y.; Guo, Y.; Wang, L.; Lu, G.; Zhan, W. Spinel structured $Co_aMn_bO_x$ mixed oxide catalyst for the selective catalytic reduction of NO_x with NH_3. *Appl. Catal. B Environ.* **2018**, *221*, 652–663. [CrossRef]

23. Husnain, N.; Wang, E.; Li, K.; Anwar, M.T.; Mehmood, A.; Gul, M.; Li, D.; Mao, J. Iron oxide-based catalysts for low-temperature selective catalytic reduction of NO_x with NH_3. *Rev. Chem. Eng.* **2019**, *35*, 239–264. [CrossRef]

24. Gao, F.; Tang, X.; Yi, H.; Zhao, S.; Li, C.; Li, J.; Shi, Y.; Meng, X. A Review on Selective Catalytic Reduction of NO_x by NH_3 over Mn–Based Catalysts at Low Temperatures: Catalysts, Mechanisms, Kinetics and DFT Calculations. *Catalysts* **2017**, *7*, 199. [CrossRef]

25. Gao, C.; Shi, J.-W.; Fan, Z.; Gao, G.; Niu, C. Sulfur and Water Resistance of Mn-Based Catalysts for Low-Temperature Selective Catalytic Reduction of NO_x: A Review. *Catalysts* **2018**, *8*, 11. [CrossRef]

26. Liu, C.; Shi, J.-W.; Gao, C.; Niu, C. Manganese oxide-based catalysts for low-temperature selective catalytic reduction of NO_x with NH_3: A review. *Appl. Catal. A Gen.* **2016**, *522*, 54–69. [CrossRef]

27. Damma, D.; Ettireddy, P.R.; Reddy, B.M.; Smirniotis, P.G. A Review of Low Temperature NH_3-SCR for Removal of NO_x. *Catalysts* **2019**, *9*, 349. [CrossRef]

28. Zeng, P.; Zhou, Z.; Liu, L.; Xu, R.; Liu, X.; Xu, M. Low temperature SCR Denitration with NH_3 via synergistic effect of highly dispersed Fe-Co sites. *Chem. Eng. J.* **2025**, *504*, 159044. [CrossRef]

29. Xin, Y.; Li, H.; Zhang, N.; Li, Q.; Zhang, Z.; Cao, X.; Hu, P.; Zheng, L.; Anderson, J.A. Molecular-Level Insight into Selective Catalytic Reduction of NO_x with NH_3 to N_2 over a Highly Efficient Bifunctional V_a-MnO_x Catalyst at Low Temperature. *ACS Catal.* **2018**, *8*, 4937–4949. [CrossRef]

30. Boningari, T.; Ettireddy, P.R.; Somogyvari, A.; Liu, Y.; Vorontsov, A.; McDonald, C.A.; Smirniotis, P.G. Influence of elevated surface texture hydrated titania on Ce-doped Mn/TiO_2 catalysts for the low-temperature SCR of NO_x under oxygen-rich conditions. *J. Catal.* **2015**, *325*, 145–155. [CrossRef]

31. Liu, J.; Li, X.; Zhao, Q.; Ke, J.; Xiao, H.; Lv, X.; Liu, S.; Tadé, M.; Wang, S. Mechanistic investigation of the enhanced NH_3-SCR on cobalt-decorated Ce-Ti mixed oxide: In situ FTIR analysis for structure-activity correlation. *Appl. Catal. B Environ.* **2017**, *200*, 297–308. [CrossRef]

32. Wang, D.; Jangjou, Y.; Liu, Y.; Sharma, M.K.; Luo, J.; Li, J.; Kamasamudram, K.; Epling, W.S. A comparison of hydrothermal aging effects on NH_3-SCR of NO_x over Cu-SSZ-13 and Cu-SAPO-34 catalysts. *Appl. Catal. B Environ.* **2015**, *165*, 438–445. [CrossRef]

33. Mu, J.; Li, X.; Sun, W.; Fan, S.; Wang, X.; Wang, L.; Qin, M.; Gan, G.; Yin, Z.; Zhang, D. Inductive Effect Boosting Catalytic Performance of Advanced $Fe_{1-x}V_xO_\delta$ Catalysts in Low-Temperature NH_3 Selective Catalytic Reduction: Insight into the Structure, Interaction, and Mechanisms. *ACS Catal.* **2018**, *8*, 6760–6774. [CrossRef]

34. Liu, F.; Shan, W.; Lian, Z.; Liu, J.; He, H. The smart surface modification of Fe_2O_3 by WO_x for significantly promoting the selective catalytic reduction of NO_x with NH_3. *Appl. Catal. B Environ.* **2018**, *230*, 165–176. [CrossRef]

35. Tan, W.; Liu, A.; Xie, S.; Yan, Y.; Shaw, T.E.; Pu, Y.; Guo, K.; Li, L.; Yu, S.; Gao, F.; et al. Ce–Si Mixed Oxide: A High Sulfur Resistant Catalyst in the NH_3–SCR Reaction through the Mechanism-Enhanced Process. *Environ. Sci. Technol.* **2021**, *55*, 4017–4026. [CrossRef] [PubMed]

36. Xie, R.; Li, K.; Tian, R.; Lu, C. Spotting d-band centers of single-atom catalysts by oxygen intermediate-boosted electrochemiluminescence. *Chem. Sci.* **2024**, *15*, 18085–18092. [CrossRef]

37. Avila-Gaxiola, J.C.; Ibarra-Armenta, J.G.; Félix-Medina, R.E.; Meza-Aguilar, S.; Demangeat, C. A magnetic map of O/Fe/Mn/Fe(0 0 1) multilayer with DFT+U scheme. *Surf. Sci.* **2022**, *718*, 122006. [CrossRef]

38. Meza-Aguilar, S.; Demangeat, C. Unraveling the effect of oxygen on the magnetic map of Fe/Cr multilayers. *Eur. Phys. J. B* **2020**, *93*, 107. [CrossRef]

39. Yao, X.; Kang, K.; Cao, J.; Chen, L.; Luo, W.; Zhao, W.; Rong, J.; Chen, Y. Enhancing the denitration performance and anti-K poisoning ability of CeO_2-TiO_2/P25 catalyst by H_2SO_4 pretreatment: Structure-activity relationship and mechanism study. *Appl. Catal. B Environ.* **2020**, *269*, 118808. [CrossRef]

40. Fang, J.; Bi, X.; Si, D.; Jiang, Z.; Huang, W. Spectroscopic studies of interfacial structures of CeO_2-TiO_2 mixed oxides. *Appl. Surf. Sci.* **2007**, *253*, 8952–8961. [CrossRef]

41. Sudarsanam, P.; Hillary, B.; Amin, M.H.; Hamid, S.B.A.; Bhargava, S.K. Structure-activity relationships of nanoscale MnO_x/CeO_2 heterostructured catalysts for selective oxidation of amines under eco-friendly conditions. *Appl. Catal. B Environ.* **2016**, *185*, 213–224. [CrossRef]

42. Yang, Y.; Qian, Y.; Li, H.; Zhang, Z.; Mu, Y.; Do, D.; Zhou, B.; Dong, J.; Yan, W.; Qin, Y.; et al. O-coordinated W-Mo dual-atom catalyst for pH-universal electrocatalytic hydrogen evolution. *Sci. Adv.* **2020**, *6*, eaba6586. [CrossRef] [PubMed]